

Article

# Structural Modifications of Single-Crystal Aragonite $\text{CaCO}_3$ Beginning at ~15 GPa: In Situ Vibrational Spectroscopy and X-ray Diffraction Evidence

Jing Gao <sup>1,\*</sup>, Yungui Liu <sup>2</sup>, Xiang Wu <sup>2</sup>, Xueyin Yuan <sup>3</sup> , Yingxin Liu <sup>4</sup> and Wen Su <sup>1</sup>

<sup>1</sup> State Key Laboratory of Lithospheric Evolution and Institutions of Earth Science, Institute of Geology and Geophysics, Chinese Academy of Sciences, Beijing 100029, China; suwen@mail.iggcas.ac.cn

<sup>2</sup> State Key Laboratory of Geological Processes and Mineral Resources, China University of Geosciences, Wuhan 430074, China; Jeannie20181010@outlook.com (Y.L.); wx780720@163.com (X.W.)

<sup>3</sup> MNR Key Laboratory of Metallogeny and Mineral Assessment, Institute of Mineral Resources, Chinese Academy of Geological Sciences, Beijing 100037, China; xueyinyuan@outlook.com

<sup>4</sup> School of Gemmology, China University of Geosciences, Beijing 100083, China; liuyingxin@cugb.edu.cn

\* Correspondence: gaojing@mail.iggcas.ac.cn

Received: 22 August 2020; Accepted: 13 October 2020; Published: 19 October 2020



**Abstract:** The structural chemistry of carbonates under mantle conditions facilitates our understanding of carbon recycling pathways in the earth's interior. It also has impacts on the dynamics of mantle–slab interactions. Aragonite is a common calcium carbonate mineral in pelagic marine sediments. The structural chemistry of single-crystal aragonite during successive compression and the behavior of a structural  $\text{H}^+$  have been investigated by micro-vibrational spectroscopy and synchrotron X-ray diffraction techniques in diamond anvil cells. We describe a reduction of the *b*-axial compressibility beginning at ~15 GPa, and the related discontinuities in the first-order derivatives of the vibrational modes. The structural modifications of aragonite are manifested by mutations occurring in the pressure relations of the wavenumbers of the O–C–O bending modes, and of the bandwidth and band intensities of the measured internal and external modes. These anomalies are indicative of changes occurring in the force constant of the C–O bonds, and possibly a second-order phase transition. Besides, the  $[\text{CaO}_9]$  polyhedra begin to deform, possibly with some Ca–O bonds becoming elongated and the others shortening. An increase in the co-ordination number for the  $\text{Ca}^{2+}$  sites could be expected under higher pressures. Additionally, the weakening of the OH modes may imply  $\text{H}^+$ -loss from the aragonite lattice above 11.5 GPa.

**Keywords:** calcium carbonate; crystal chemistry; OH bands; diamond anvil cell

## 1. Introduction

Plate tectonics theory outlines the subduction process of the oceanic lithosphere at the interface of convergent plates [1]. Geophysical observations [2] and mineralogical evidence [3] extend the subduction region to the 660 km discontinuity and depict the retention of slabs at the topmost of the lower mantle. By the subduction processes, sedimentary carbonates are transported into the earth. As a vital carrier of carbon, carbonates play a key role in connecting surficial volatiles with those in the earth's interior, which helps maintain a habitable environment [4,5]. Studies on the high-pressure behaviors of carbonates provide fundamental information for our understanding on decarbonation reactions under upper mantle conditions [6]. Besides, existence of carbonates in the Earth's mantle decreases the melting point of mantle peridotite and promotes partial melting. This provides a predisposition for geochemical and geophysical anomalies locally or planet differentiation on a large scale [7]. In consideration of the relative coldness of the subducted slabs at subarc depths [8], a certain amount of carbonates would

survive from consumption reactions (e.g., decarbonation, dissolution, melting or interactions with surrounding silicates) at the early stage of subduction and migrate to deeper regions [9]. The crystal chemistry of carbonates under deep mantle conditions exerts a significant effect on the geophysics of the slab and the dynamics of mantle–slab interactions [10,11]. For instance, pressure-induced phase transitions of calcium carbonates changes shear sound velocities [11], offering insights into the seismic discontinuities detected at the depth around 700 km in the vicinity of the sinking slabs [12]. Moreover, the subducted carbonates are accepted as carbon sources and parental media of sublithospheric diamonds (crystallized at depths in excess of 300 km) [13–16]. Carbon reduction pathways from surficial carbonates to diamonds do not merely relate to the dynamics of Earth carbon recycling but are a good lead indicator of the variation of oxygen fugacity along subduction geotherms. So, the high-pressure crystal chemistry of carbonates has been a hot topic for decades.

Aragonite  $\text{CaCO}_3$  (*Pm $\bar{c}$ n* and  $Z = 4$ ) is a common calcium carbonate mineral in pelagic marine sediments. It shows a greater stability over its homomorphic polymorph, calcite (*R-3c* and  $Z = 6$ ), above 0.3–2 GPa [17,18]. Aragonite had long been considered a stable  $\text{CaCO}_3$ -polymorph in the earth's interior from megapascals regimes to the lower mantle. However, more and more scholars put forward different views on its stability. An early shock compression experiment has suggested a displacive phase transition of aragonite at 5.5–7.6 GPa and possibly another at ~16 GPa [19]. These observations are, however, inconsistent with subsequent studies. Kraft et al. [20] and Gillet et al. [21] insist that aragonite persists to at least ~30 GPa using vibrational spectroscopic techniques, in line with theoretical results [17,18,22]. Upon higher pressures, Santillán and Williams observe a strong lattice strain of aragonite through the X-ray diffraction (XRD) technique. The occurrence of the lattice strain may mark the onset of a sluggish transition to a trigonal structure at 35–40 GPa [23]. Soon afterwards, however, Ono et al. [24] dismiss the trigonal structure but are in favor of an orthorhombic structure, post-aragonite, with the space group of *P2<sub>1</sub>2<sub>1</sub>2* and  $Z = 2$ . Discordant with the experimental results, attempts using theoretical methods declare that the space group of post-aragonite is *Pm $\bar{m}$ n* and  $Z = 2$  [17,18,25]. Recent advances using calculations and the XRD technique demonstrate that aragonite stabilizes until 35 GPa, above which, a distorted aragonite structure named aragonite-II sets in [26,27]. Simultaneously, a monoclinic structure termed  $\text{CaCO}_3$ -VII (*P2<sub>1</sub>/c-1* and  $Z = 4$ ) has been suggested to be more energetically favorable under pressures of 23–50 GPa in an extensive temperature range of 300–2500 K [11,22,26–29].  $\text{CaCO}_3$ -VII could be considered an intermediate phase in the transformation from aragonite to post-aragonite [22,28].

Previous studies provoke a long-term debate on the structural stability and phase transitions of aragonite upon pressure. Regardless of controversies, these studies using the powder sample generally believe that aragonite preserves stable to the topmost of the lower mantle (~25–30 GPa), where it transforms to  $\text{CaCO}_3$ -VII and further to post-aragonite at ~40–45 GPa with weak Clapeyron slopes (Figure 1). However, a single-crystal specimen is much more sensitive to the changes of pressure than powder. Single-crystal XRD is a useful technique to identify structure of materials, which proves to improve high-pressure phase diagrams determined by powder samples [30,31]. An intensive study using a single-crystal specimen of calcium carbonate proposes a triclinic structure  $\text{CaCO}_3$ -VI (*P-1* and  $Z = 2$ ) above 15 GPa [32]. This structure is likely to be the same as that observed but not identified in a dynamic compression experiment [19]. Instead of a phase transition, however, the reduction of the *b*-axis compressibility is identified in aragonite at the same pressure in a recent single-crystal XRD research [33]. Currently whether aragonite undergoes a transformation at the bottom of the upper mantle or stabilizes but develops an axial stiffness remains an open issue. Besides, stiffness of axes is particularly intriguing because it associates closely to the distortion of polyhedra and probably triggers structural changes under higher pressures. For this purpose, a combination of Raman Spectroscopy and Fourier Transform Infrared Spectroscopy (FTIR) techniques has been utilized to yield the structural changes of single-crystal aragonite from atmospheric pressure to ~24 GPa. Because infrared and Raman spectroscopy could provide crystal-structure information at the molecular level and the bonds with different chemical and local environment have different pressure responses, we expect to find the

systematic shifts of the external/internal mode wavenumbers by successive compression experiments. Besides, with the improvement of analytical technique, the study of vibrational modes of a material becomes more precise. Thus we could find the emergence of subtle changes that might have been overlooked previously. Prior to the micro-vibrational measurements, synchrotron XRD experiments have been performed to monitor the overall structural changes of aragonite up to 27.1 GPa. It is known that different pressure media may lead to different results; thus, we check the high-pressure behavior of aragonite at various hydrostatic conditions by using various pressure media in the XRD, infrared and Raman spectroscopy measurements. These results will facilitate our knowledge of the crystal chemistry of aragonite upon pressure. This is fundamental to disclose carbon recycling pathways during subduction processes and evaluate its effects on the physicochemical properties of the surrounding mantle.

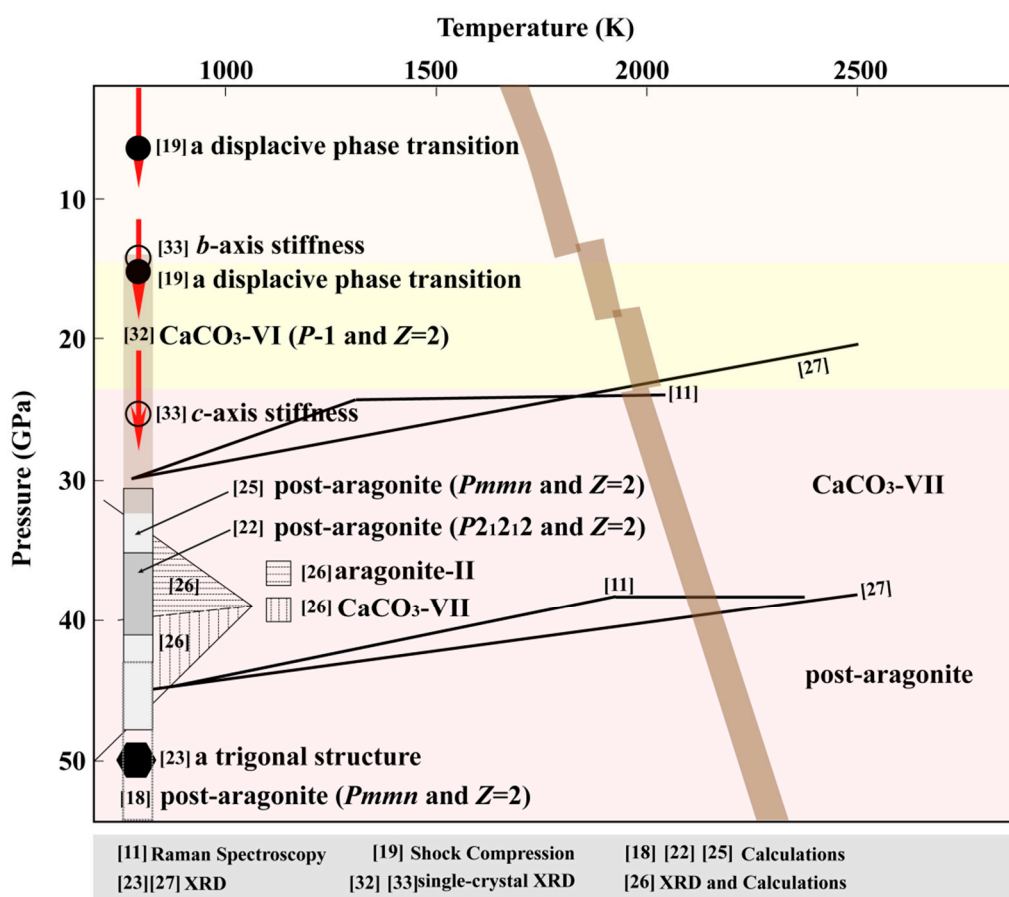


**Figure 1.** Phase diagram of CaCO<sub>3</sub> under mantle conditions. The solid black lines depict the phase boundaries as labeled. Two studies using single-crystal specimen of aragonite have detected a phase transition or a reduction in the *b*-axis compressibility at ~15 GPa, respectively. The light gray zone indicates the mantle geotherm [34]. The dotted arrow represents the experimental conditions presently.

## 2. Materials and Methods

### 2.1. Sample Description

A natural single-crystal of aragonite, crackless and transparent, formed in a pseudohexagonal columnar crystalline morphology, was selected for the high-pressure measurements. Qualitative chemical analyses have been undertaken on a Scanning Electron Microscope (SEM) by the method of Energy Dispersive Spectroscopy (EDS) at the Institute of Geology and Geophysics, Chinese Academy of Science (IGGCAS), Beijing, China. Little impurity was detected except for

Ca, C and O atoms present in the ideal  $\text{CaCO}_3$  formula. The crystal structure of the sample was characterized using the X-ray diffraction (XRD) technique at the Institute of Tibetan Plateau Research, Chinese Academy of Sciences (ITPCAS), Beijing, China. The XRD pattern indicates an orthorhombic system ( $Pm\bar{c}n$  and  $Z = 4$ ) with the values of the lattice constants of  $a_0 = 4.9618(2) \text{ \AA}$ ,  $b_0 = 7.976(2) \text{ \AA}$ ,  $c_0 = 5.742(2) \text{ \AA}$  and  $V_0 = 226.9(1) \text{ \AA}^3$ , in agreement with the results for aragonite from previous studies [33,35–39]. Prior to the high-pressure measurements, the aragonite crystal had been dried at  $110 \text{ }^\circ\text{C}$  overnight to remove possible absorbed water on the surface.

## 2.2. Single-Crystal X-ray Diffraction (XRD)

A short-symmetric diamond-anvil cell (DAC) equipped with Boehler-Almax diamond anvils of  $380 \text{ }\mu\text{m}$  culets was employed for synchrotron single-crystal XRD experiments. A hole of  $260 \text{ }\mu\text{m}$  in diameter was drilled in a pre-indented rhenium gasket of  $36 \text{ }\mu\text{m}$  in thickness as the sample chamber. An aragonite crystal with the grain size approximately  $20 \times 30 \times 15 \text{ }\mu\text{m}^3$  was loaded in the chamber, along with a piece of platinum for pressure calibration, which provides pressure accuracy within  $0.1 \text{ GPa}$  [40]. High-purity Ne gas was loaded into the chamber at room temperature via a COMPRES/GSECARS gas loading apparatus and a ruby sphere was used as an initial pressure indicator [41,42].

In situ high-pressure XRD patterns were measured at beamline 13-BM-C at Advanced Photon Source (APS), Argonne National Laboratory (ANL), Chicago, IL, USA. A monochromatic X-ray beam with the wavelength of  $0.43409 \text{ \AA}$  was focused on a  $15 \times 15 \text{ }\mu\text{m}^2$  spot. XRD images were collected during the continuous rotation of the cell from  $-33^\circ$  to  $+33^\circ$ . The Pilatus3 1M detector parameters were calibrated by a  $\text{LaB}_6$  standard, and integration to conventional  $2\theta$ -intensity data was carried out using Dioptas software. The indexing and refinement of the patterns were performed by a unitcell program package.

## 2.3. Fourier Transform Infrared Spectroscopy (FTIR)

A symmetric DAC equipped with ultra-low-fluorescence diamonds (IIa type) of  $400 \text{ }\mu\text{m}$  culet diameter was used for FTIR measurements. An aragonite crystal of  $25 \text{ }\mu\text{m}$  thickness, sandwiched by two dried KBr layers that served as an infrared window and a pressure transmitting medium, was enclosed in a  $200 \text{ }\mu\text{m}$  diameter hole in a  $45 \text{ }\mu\text{m}$  thickness rhenium gasket. Pressure was determined by a ruby fluorescence method [41], which provides a pressure accuracy of  $0.1 \text{ GPa}$  below  $14 \text{ GPa}$  and  $0.2 \text{ GPa}$  thereafter.

In situ high-pressure FTIR spectra were collected using a Bruker VERTEX 70V instrument at IGGCAS, Beijing, China. A HeNe lamp was used as the light source to cover a spectral range of  $650\text{--}4500 \text{ cm}^{-1}$ , coupled with a liquid nitrogen cooled Mercury-Cadmium-Telluride (MCT) detector. A Bruker Hyperion 2000 microscope with a  $10\times$  objective was used to focus the beam on the sample inside the cell. Each spectrum was measured with a spectral resolution of  $4 \text{ cm}^{-1}$  and presents an average over 640 scans after normalization against a background spectrum on an area of KBr in the cell at the same pressure, with a total acquisition time of 550 s. Preliminary data processing was done by the Opus software package through a Lorentz model.

## 2.4. Raman Spectroscopy

High-pressure polarized Raman spectroscopy were conducted using the same symmetric cell with silicone oil as the pressure medium. The scattered Raman signal was measured through a WITec alpha 300R instrument (WITec, Ulm, Germany) equipped with a  $532 \text{ nm}$  solid-state laser. A long-distance ZEISS  $50\times$  lens ( $\text{NA} = 0.55$ ) was used with a  $600 \text{ grooves/mm}$  grating and the spectral resolution of  $2.4 \text{ cm}^{-1}$ . The Raman spectra were collected at a laser power of  $12 \text{ mW}$ , an acquisition time of  $2 \text{ s}$  and an accumulation of 5. Data analyses were performed through the WITec Project 5.2 program (WITec, Ulm, Germany).

### 3. Results and Discussions

#### 3.1. X-ray Diffraction of Aragonite up to 27.1 GPa

The single-crystal XRD patterns of aragonite have been collected with pressure increasing up to 27.1 GPa. The pressure-dependent unit cell parameters derived from the diffraction data are listed in Table 1, with the relations plotted in Figure 2. No observable discontinuities are observed in the volume relation, which indicates that aragonite maintains stability in the present conditions. This is consistent with the findings of most previous studies [11,18,20–29,33]. A least-square fit of the compression data to the third-order Birch–Murnaghan equation of state (BM EoS) yields the values of the bulk modulus of the volume to be  $B_0 = 71(5)$  GPa,  $B_0' = 4.3(4)$  and  $V_0 = 228.3(8)$  Å<sup>3</sup>, in accordance with the values obtained by XRD [33,38] and Brillouin spectroscopy measurements [39].

**Table 1.** Aragonite unit-cell parameters and volume up to 27.1 GPa.

Pressure (GPa)	<i>a</i> (Å)	<i>b</i> (Å)	<i>c</i> (Å)	<i>V</i> (Å <sup>3</sup> )
0.9	4.960(7)	7.921(4)	5.719(2)	224.9(3)
2.6	4.932(7)	7.899(4)	5.667(2)	220.8(3)
4.8	4.902(7)	7.834(4)	5.589(2)	215.9(3)
7.6	4.859(7)	7.794(4)	5.515(2)	210.6(3)
10.1	4.812(6)	7.734(4)	5.464(2)	204.4(2)
11.9	4.798(6)	7.707(4)	5.424(2)	201.3(2)
12.9	4.779(6)	7.683(4)	5.378(2)	200.0(2)
13.7	4.770(6)	7.672(4)	5.357(2)	198.1(2)
16.4	4.749(6)	7.661(4)	5.306(2)	195.4(2)
19.2	4.729(6)	7.648(4)	5.246(2)	191.6(2)
21.6	4.709(6)	7.629(4)	5.195(1)	188.8(2)
23.5	4.691(6)	7.611(4)	5.148(1)	186.4(2)
25.3	4.678(6)	7.607(4)	5.112(1)	184.0(2)
27.1	4.666(6)	7.603(4)	5.078(1)	182.2(2)

In the pressure cycle, the *a*- and *c*-axis length decrease continuously. The *c*-axis exhibits similar compressibility to that reported previously [33,37], but the *a*-axis shows a little higher compressibility. This can be accounted for by the differences in the chemical compositions, crystal orientations and/or pressure media used (different hydrostatic conditions) [43]. Besides, it should be noted that the H<sup>+</sup> incorporated in nominally anhydrous minerals (NAMs) has significant effects on the chemical and physical properties. So, the effects of the structural H<sup>+</sup> (see the infrared spectra below) on the axial compressibility cannot be excluded. The value of the modulus of the *a*-axis, calculated through the modified BM EoS, is 141(3) GPa (and  $B_0' = 4.99(1)$ ), nearly triples 53(2) GPa (and  $B_0' = 2.26(9)$ ) of the *c*-axis. The high degree of axial compression anisotropy is due mainly to the structure feature. The aragonite structure is constituted by the coplanar [CO<sub>3</sub>]<sup>2-</sup> triangles parallel to the *ab*-plane and the [CaO<sub>9</sub>] polyhedra arranging along the *c*-axis. The [CO<sub>3</sub>]<sup>2-</sup> units are rigid in comparison with the [CaO<sub>9</sub>] polyhedra, and the [CaO<sub>9</sub>] polyhedra have longer Ca–O bonds along the *c*-axis yet shorter in the *ab*-plane. As a consequence, the whole structure displays a compressible *c*-axis relative to a hard *ab*-plane.

In spite of the continuous relations above, the fitting of the *b*-axis parameter to the modified EoS, unexpectedly, cannot converge. A closer examination leads us to find that the data above 15 GPa become less varied. Therefore, we describe the *b*-axis length in the pressure range of 0.9–13.7 GPa and 16.4–27.1 GPa, respectively. The obtained value of the modulus of the *b*-axis is 116(9) GPa below ~15 GPa, but it increases sharply to 333(42) GPa thereafter. The stiffness of the *b*-axis has been overlooked by most XRD attempts using powder specimen, but identified in a single-crystal XRD study by Palaich et al. [33]. The compressibility of the *b*-axis above ~15 GPa obtained here is a little different from that in Palaich et al. [33]. This discrepancy can be accounted for by the difference in the orientation of aragonite crystal and/or in the chemical composition (e.g., structural H<sup>+</sup>) of the

aragonite specimen. Previously, Merlini et al. [32] has identified a triclinic structure  $\text{CaCO}_3\text{-IV}$  above 15 GPa which is transformed from calcite.  $\text{CaCO}_3\text{-IV}$  has a higher density than aragonite yet with a lower co-ordination number for the Ca sites. In the present study, no sign of formation of  $\text{CaCO}_3\text{-IV}$  is detected. So, we assume a superior structural stability of aragonite over  $\text{CaCO}_3\text{-IV}$  above 15 GPa. The stiffness of the  $b$ -axis indicates the onset of subtle structural modifications along the  $b$ -axis, but no more information can be gained from the XRD data [33]. Some fine structural information is much easier to capture by vibrational spectroscopy rather than XRD due to the strong pressure dependence of the mode wavenumbers, full width at half maximum (FWHM) and intensities of changes in interatomic distances that are subtle in the XRD patterns [44]. Thus, we conduct in situ high-pressure FTIR and Raman spectroscopy measurements in the following.

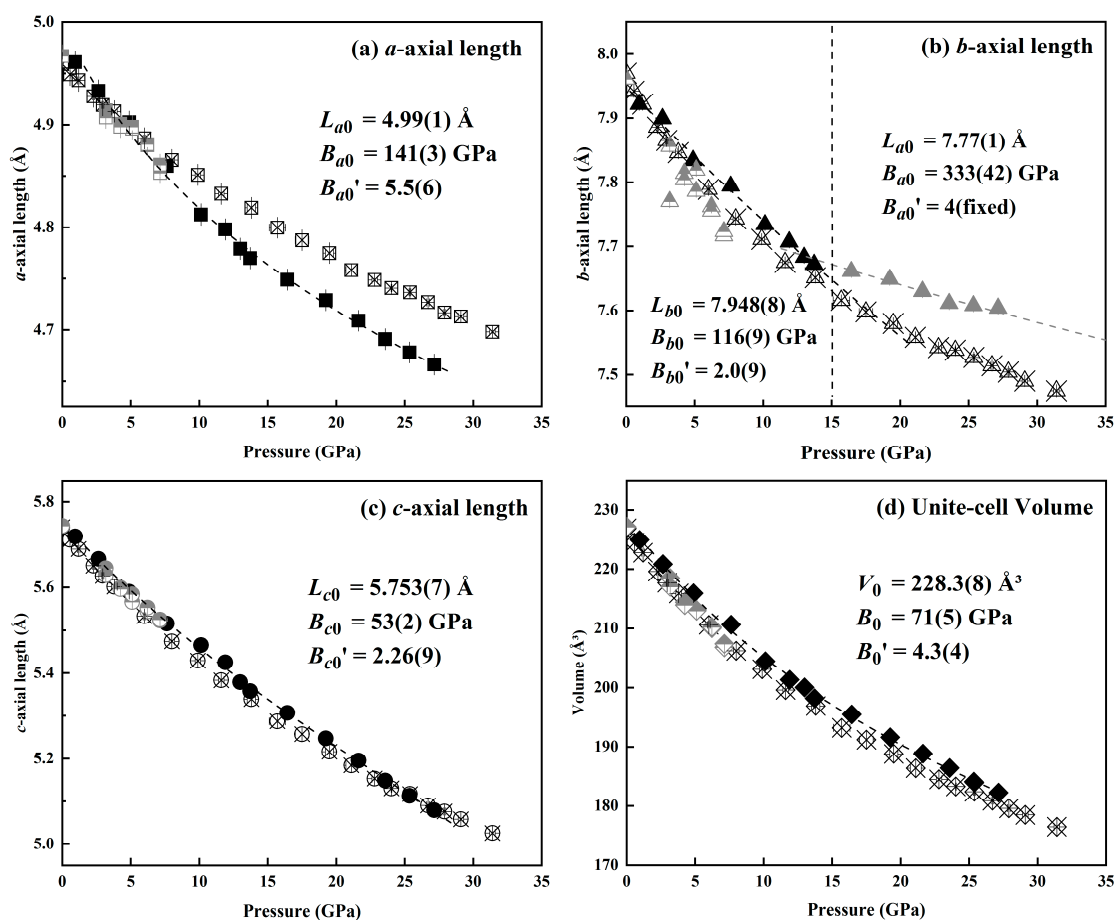


**Figure 2.** Lattice parameters of aragonite derived from X-ray diffraction (XRD) patterns upon pressure. The uncertainty in the value is generally smaller than the symbol size. The dashed black curve represents the fit of the data to the third-order Birch–Murnaghan equation of state (BM EoS). The XRD data referred from Palaich et al. [33] (symbols with a cross in the center) and from Martinez et al. [36] (half-closed symbols) are plotted for comparison.

### 3.2. Vibrational Spectra of Aragonite at Ambient Conditions

Theoretically, the symmetry of the optic modes of aragonite is describable as:

$$\text{Total} = 9A_g(\text{R}) + 6B_{1g}(\text{R}) + 6B_{2g}(\text{R}) + 9B_{3g}(\text{R}) + 6A_u(\text{I}) + 8B_{1u}(\text{IR}) + 8B_{2u}(\text{IR}) + 5B_{3u}(\text{IR}) \quad (1)$$

It consists of 21 IR-active (Infrared Spectroscopy, IR), 30 Raman-active (R) and 6 inactive modes. Presently, 19 IR and eight R modes are observed (Figure 3) belonging to three spectral groups [20,36,45,46]: (1) internal modes in the range of  $600\text{--}1600 \text{ cm}^{-1}$ , (2) external modes in the

50–350  $\text{cm}^{-1}$  region and (3) overtone bands over 1700–3000  $\text{cm}^{-1}$ . For internal modes, a diagnostic band at  $\sim 1083 \text{ cm}^{-1}$  arises from O-C-O symmetrical stretching vibration ( $\nu_1$ ). Due to the lower site group symmetry surrounding the  $[\text{CO}_3]^{2-}$  units, the in-plane O-C-O bending mode ( $\nu_4$ ) splits into two components positioned at 700.21(2) and 712.88(5)  $\text{cm}^{-1}$ . It is also the case with the asymmetric stretching mode ( $\nu_3$ ), which is manifested by a broad band over wavenumbers of 1300–1600  $\text{cm}^{-1}$  that involves splittings of transverse and longitudinal components (Figure 3a). Likewise, the out-of-plane vibration ( $\nu_2$ ) is featured by three splitted bands centered at 842.36(2), 856.47(3) and 868.87(2)  $\text{cm}^{-1}$ , respectively. In addition, an overtone band with the mode wavenumber close to the combination of  $\nu_2$  and  $\nu_2$  is present at 1790  $\text{cm}^{-1}$ . The other one of  $\nu_1$  plus  $\nu_3$  is around 2555  $\text{cm}^{-1}$ . Besides, the Raman spectrum (Figure 3b) presents four external modes,  $\nu_{E1}$ ,  $\nu_{E2}$ ,  $\nu_{E3}$  and  $\nu_{E4}$ , due to the rotations and translations of the  $[\text{CO}_3]^{2-}$  units or the vibrations of the Ca-O bonds. The polarized Raman spectrum of aragonite collected here accords with that in Kraft et al. [20] and Carteret et al. [35]. Additionally, three bands standing at wavenumbers of 3400–3600  $\text{cm}^{-1}$  are clearly identified (Figure 3a), which could be interpreted as resulting from the stretching vibration of structural OH. The two modes at  $\sim 2300 \text{ cm}^{-1}$  are due to gaseous (atmospheric)  $\text{CO}_2$ . There stand three bands at 2800–3000  $\text{cm}^{-1}$ , which have been observed and assigned to C-H vibrations by previous studies [47]. This may come from organic impurities on the surface of the sample crystal. Presently, we focus on the pressure dependence of the internal modes ( $\nu_1$ ,  $\nu_2$ ,  $\nu_4$ ), external modes ( $\nu_{E1}$ ,  $\nu_{E2}$ ,  $\nu_{E3}$ ) and OH vibrations.

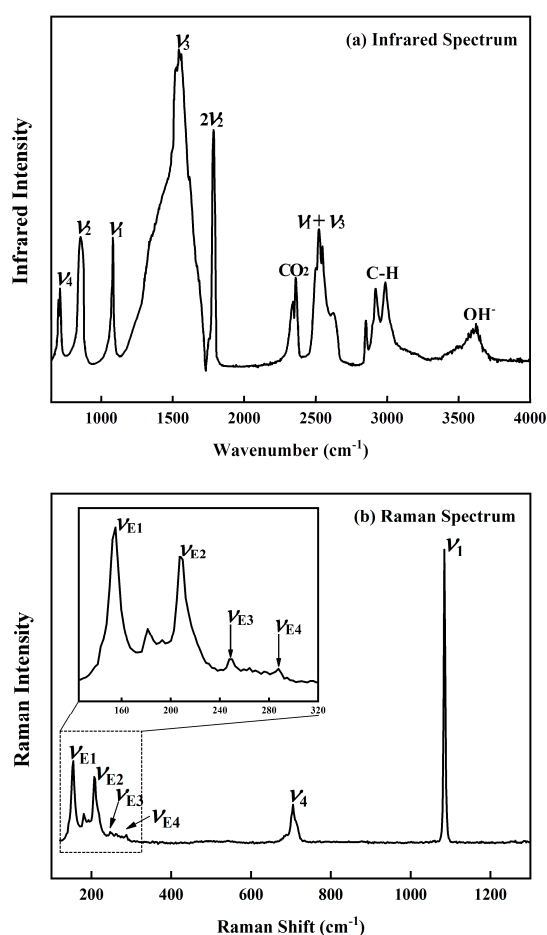


**Figure 3.** (a) Infrared and (b) Raman spectrum of aragonite at ambient conditions corrected for background effects.

### 3.3. Vibrational Spectra of Aragonite upon Pressures below 15 GPa

Representative infrared and Raman spectra of aragonite during compression are illustrated in Figure 4, each with a pressure-released spectrum plotted at the bottom. To explore the pressure dependence of the vibrational modes in detail, we derive the band positions, bandwidth and the intensities of the main external/internal modes under various pressures (Tables 2 and 3). The majority of the measured modes exhibit a systematic increase of peak positions upon pressure. For example, the two  $\nu_4$  bands blue-shift progressively at a linear slope ( $\delta\nu/\delta P$ ) of  $1.42(1) \text{ cm}^{-1}\cdot\text{GPa}^{-1}$  for the  $700.21(2) \text{ cm}^{-1}$  band and  $1.95(4) \text{ cm}^{-1}\cdot\text{GPa}^{-1}$  for  $712.88(5) \text{ cm}^{-1}$  (Figure 5a). Due to the difference in the pressure coefficient, the two  $\nu_4$  bands display an increasing separation with increasing pressure. Kraft et al. [20] and Gillet et al. [21] have, respectively, reported the splitting of the two  $\nu_4$  bands of aragonite upon pressure. To the best of our knowledge, this increased splitting has arisen from two effects: an increasing asymmetry of the local crystal field of the  $[\text{CO}_3]^{2-}$  unit and the distortion of the  $[\text{CO}_3]^{2-}$  unit itself. White [45] has contended that, in carbonates, the distortion of the  $[\text{CO}_3]^{2-}$  units plays a role in the magnitude of the site-group splitting. Especially for aragonite, the C-O bond length and the O-C-O angle grow more unidentical in the course of compression [20,33,38]. As a result, we infer that the increased splitting of the  $\nu_4$  components under compression could be accounted for by the substantial angular and spacing variations of O-C-O.

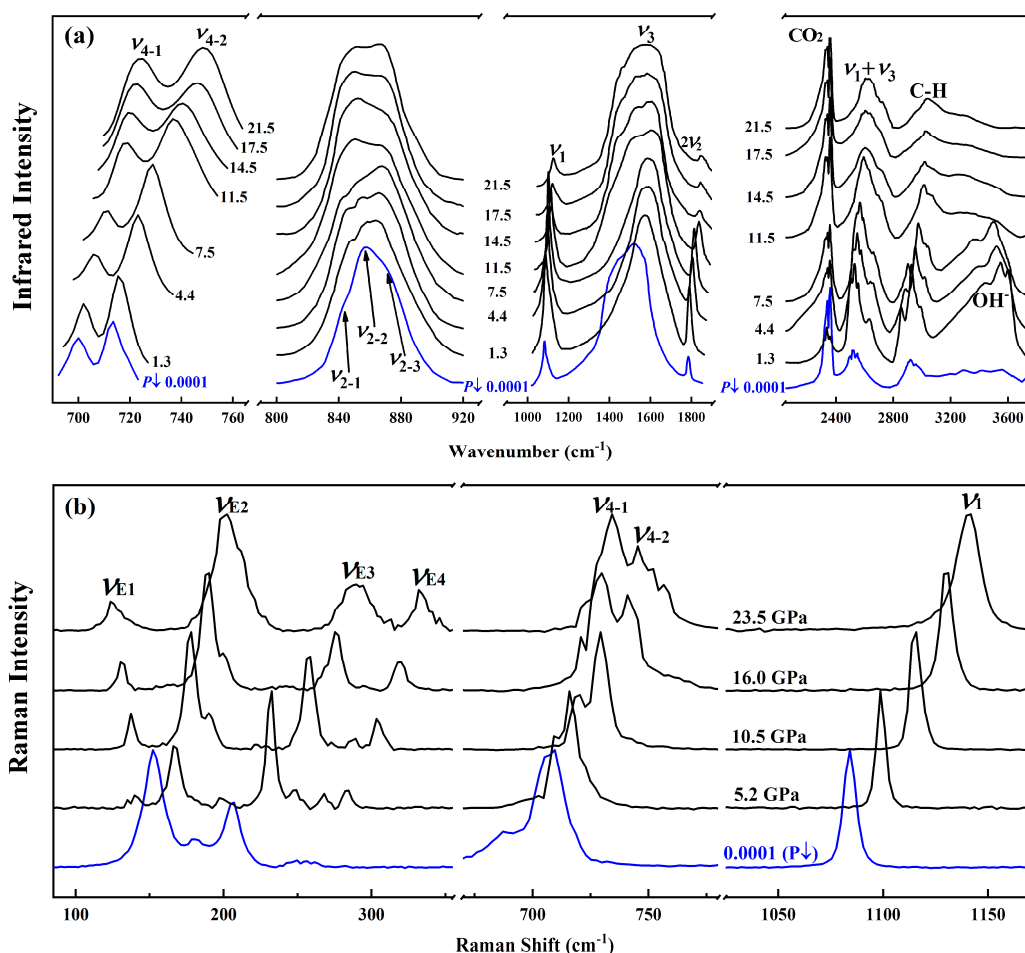


**Figure 4.** (a) Infrared and (b) Raman spectra of aragonite as a function of pressure with the background subtracted. The spectra labeled by P↓ was collected after decompression. In (b), the scale of the lower-wavenumber data ( $< \sim 800 \text{ cm}^{-1}$ ) has been trebled for greater clarity.

**Table 2.** Wavenumber, full width at half maximum (FWHM) and intensity of infrared modes of aragonite versus pressure.

Pressure (GPa)	$\nu_{4-1}$			$\nu_{4-2}$			$\nu_2$			$\nu_{OH}$		
	Wavenumber ( $\text{cm}^{-1}$ )	FWHM ( $\text{cm}^{-1}$ )	Intensity (Counts)	Wavenumber ( $\text{cm}^{-1}$ )	FWHM ( $\text{cm}^{-1}$ )	Intensity (Counts)	Wavenumber ( $\text{cm}^{-1}$ )			Wavenumber ( $\text{cm}^{-1}$ )		
0.0001●	700.21(2)	3.23(5)	53,045(625)	712.88(5)	7.87(2)	118,883(928)	842.36(2)	856.47(3)	868.87(2)			
0.0001 (P↓)	700.54(6)	3.62(3)	65,135(742)	713.11(3)	7.97(5)	119,105(833)	843.61(3)	857.26(4)	869.28(4)			
1.3	702.23(5)	9.05(3)	52,855(533)	715.81(2)	10.80(6)	102,445(863)	844.25(4)	856.30(2)	867.39(2)	3399.19(2)	3541.16(6)	3606.41(1)
2.3	703.66(3)	8.74(2)	40,114(528)	718.34(5)	11.40(3)	115,321(631)	843.35(2)	855.24(3)	868.19(6)	3394.22(1)	3530.50(1)	3600.23(2)
3.5	705.59(5)	9.77(6)	46,036(631)	720.37(6)	11.65(6)	95,356(742)	842.58(5)	853.64(3)	867.23(2)	3388.58(6)	3524.58(6)	3589.31(4)
4.4	706.28(6)	10.50(5)	32,201(561)	722.86(1)	12.68(3)	86,498(849)	842.98(4)	854.87(4)	868.23(3)	3380.79(2)	3515.44(6)	3587.23(6)
5.5	708.33(2)	10.59(6)	36,262(763)	724.29(2)	12.67(6)	85,205(561)	842.27(5)	852.27(2)	868.06(5)	3374.15(1)	3508.65(1)	3579.61(7)
6.4	709.68(3)	12.14(2)	34,324(831)	726.72(1)	13.50(1)	72,669(763)	841.50(3)	852.38(5)	867.56(4)	3368.15(5)	3503.28(5)	3577.74(7)
7.5	711.19(1)	12.31(5)	29,625(731)	728.21(1)	14.73(2)	64,652(628)	841.65(3)	851.15(6)	868.69(6)	3359.49(6)	3496.99(7)	3571.05(5)
8.5	712.20(2)	13.52(3)	32,568(649)	730.92(5)	16.22(6)	51,912(729)	840.44(2)	851.01(2)	867.51(3)	3355.12(2)	3491.81(6)	3565.48(1)
9.5	713.53(5)	15.47(6)	27,842(463)	732.31(6)	17.43(1)	58,946(561)	842.62(5)	852.52(5)	868.59(5)	3350.50(6)	3490.91(2)	3561.20(4)
10.5	715.06(2)	15.20(1)	24,104(561)	735.02(3)	18.22(3)	58,643(549)	841.53(4)	850.60(2)	866.62(4)	3344.05(1)	3488.59(1)	3557.30(2)
11.5	717.09(3)	16.99(6)	22,518(442)	736.61(3)	19.24(2)	47,827(633)	842.21(4)	851.83(4)	867.24(6)			
13.4	719.38(6)	19.30(2)	24,095(633)	739.35(5)	22.15(5)	62,242(525)	840.24(2)	851.45(4)	868.42(2)			
14.5	721.09(5)	20.10(3)	24,095(725)	741.76(3)	23.13(3)	53,516(631)	841.06(3)	851.53(3)	867.10(4)			
17.5	722.99(2)	21.07(6)	47,782(731)	745.24(6)	24.26(6)	70,728(528)	839.54(4)	850.81(2)	867.25(4)			
21.5	725.18(6)	19.48(5)	46,558(763)	748.17(5)	25.28(1)	56,595(649)	840.62(2)	851.33(5)	866.64(3)			

0.0001● refer to the data collected at ambient conditions outside diamond anvil cell. 0.0001 (P↓) represent the data obtained after decompression within DAC. The number in the parentheses represents one standard deviation in the right-most digit.

**Table 3.** Experimentally determined Raman mode wavenumber, FWHM and intensity of aragonite as a function of pressure.

Pressure (GPa)	$\nu_{E2}$			$\nu_{E3}$			$\nu_1$		
	Wavenumber ( $\text{cm}^{-1}$ )	FWHM ( $\text{cm}^{-1}$ )	Intensity (Counts)	Wavenumber ( $\text{cm}^{-1}$ )	FWHM ( $\text{cm}^{-1}$ )	Intensity (Counts)	Wavenumber ( $\text{cm}^{-1}$ )	FWHM ( $\text{cm}^{-1}$ )	Intensity (Counts)
0.0001●	152.8(1)	8.0(1)	3012(66)	205.5(1)	10.2(2)	2965(68)	1082.19(1)	3.63(2)	4268(48)
0.8	154.2(2)	9.2(7)	2952(78)	208.8(3)	13.2(9)	3064(131)	1084.97(1)	4.33(4)	4826(52)
2.0	159.6(2)	7.0(7)	1837(80)	217.9(1)	8.23(3)	2660(93)	1090.56(2)	4.53(7)	3300(38)
5.2	167.2(2)	7.4(7)	1356(95)	232.0(1)	6.3(3)	2246(93)	1098.99(1)	5.00(4)	4187(40)
7.5	173.4(2)	10.0(8)	1247(98)	245.0(1)	5.7(3)	1842(81)	1107.37(1)	4.92(4)	5413(59)
10.5	177.8(1)	9.6(6)	1168(97)	257.6(2)	8.3(6)	1621(97)	1115.40(4)	5.44(12)	5519(138)
12.5	181.5(1)	9.0(5)	1435(65)	265.5(1)	7.3(3)	1510(56)	1121.44(4)	5.88(11)	3263(73)
14.2	185.7(1)	9.1(4)	1937(77)	270.2(1)	7.2(3)	1642(66)	1124.46(2)	6.26(8)	4085(62)
16.0	189.3(1)	10.1(4)	2327(74)	275.8(2)	9.5(7)	1802(70)	1128.03(2)	6.38(7)	5384(64)
17.5	193.6(1)	12.6(5)	2600(96)	280.5(5)	15.0(9)	1981(97)	1130.27(2)	7.03(8)	3800(40)
19.0	195.9(1)	15.2(6)	3080(100)	281.6(8)	22.3(10)	2191(122)	1132.53(2)	8.30(10)	4206(34)
20.5	198.6(2)	18.8(7)	3509(99)	288.1(9)	28.0(10)	2558(143)	1135.16(2)	9.74(9)	8270(86)
23.5	203.2(2)	23.6(9)	3845(94)	290.4(6)	41.0(11)	3270(108)	1140.52(6)	13.27(23)	6909(149)
20.0	200.7(2)	21.6(9)	3703(94)	287.2(5)	32.4(12)	3038(160)	1138.20(5)	11.77(20)	8849(159)
17.5	196.8(2)	20.7(9)	3807(104)	279.2(7)	28.2(13)	3205(163)	1132.84(6)	9.82(25)	8354(301)
4.5	168.9(1)	17.8(8)	4897(131)	229.8(3)	21.7(10)	3825(125)	1096.16(2)	6.58(8)	5389(84)
0.0001 (P↓)	153.0(2)	17.4(9)	6343(142)	205.0(4)	16.9(10)	4068(193)	1082.63(1)	5.09(4)	4722(35)

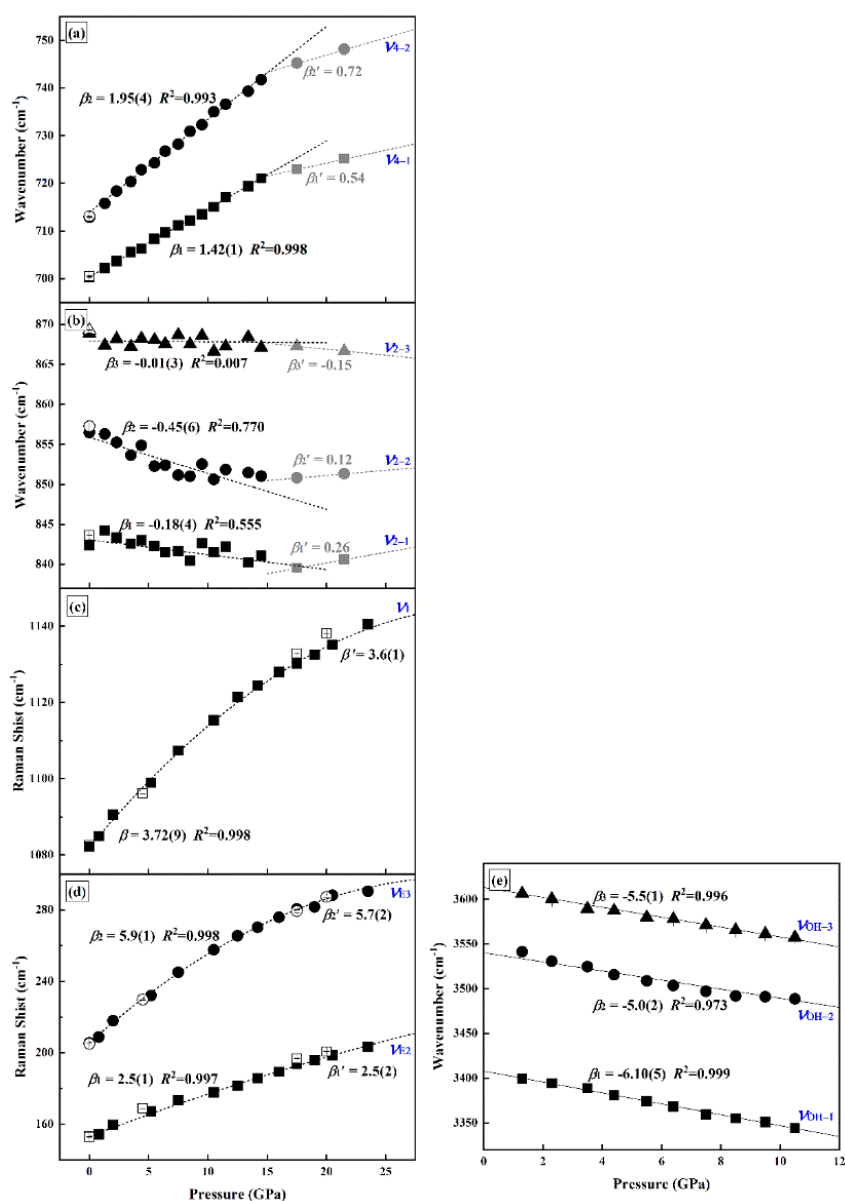


**Figure 5.** Mode wavenumbers versus pressure plot for aragonite. The relations in (a) in-plane O-C-O bending modes, (b) out-of-plane O-C-O bending modes and (e) the stretching vibration of OH are derived from the infrared spectra and in (c) O-C-O symmetrical stretching vibration and (d) O-C-O asymmetric stretching vibration from the Raman data. The closed/open symbols denote data measured during the upward/downward cycle of pressure. Symbol size generally exceeds the estimated standard deviations of the mode wavenumber. The dotted curves are the least square fittings to the data.

Different from  $\nu_4$ , the  $\nu_2$  mode wavenumbers exhibit much smaller variations upon compression (Figure 5b). The linear pressure coefficients are yielded as  $-0.18(4)$ ,  $-0.45(6)$  and  $-0.01(3)$   $\text{cm}^{-1}\cdot\text{GPa}^{-1}$ , respectively, for  $842.36(3)$ ,  $856.47(3)$  and  $868.87(2)$   $\text{cm}^{-1}$ . The negative pressure dependence is a generic property of most carbonate minerals and has been suggested to be resulted from an increasing strength of the Ca-O bond upon pressure [20,21,46]. The integral absorbance of the three  $\nu_4$  bands, which originally decreases in the order of  $868.8 > 856.4 > 842.3$   $\text{cm}^{-1}$ , reverses above 11.5 GPa. It is known that the out-of-plane bending modes exhibit strong pressure dependence of the intensity on the internal stress. Given that no anomalies are detected in the XRD patterns or the Raman spectra at similar pressures, we attribute the variations in the mode intensities to the pressure gradient generated within the KBr medium and the associated occurrence of shear strains within the sample.

The  $\nu_1$  mode shifts to higher wavenumbers along a continuously quadratic pattern (Figure 5c). This indicates that the main characteristics of the  $[\text{CO}_3]^{2-}$  units are unchanged. The shift rate reduces in a stepwise manner from 3.72(9) at atmospheric pressure to 3.6(1)  $\text{cm}^{-1}\cdot\text{GPa}^{-1}$  at 23.5 GPa. Even though the  $[\text{CO}_3]^{2-}$  unit behaves as a rather rigid group, the high wavenumber modes generally show a greater increase in wavenumber as pressure is increased.

The external modes,  $\nu_{E2}$  and  $\nu_{E3}$ , blue-shift along quadratic patterns continuously, whereas the  $\nu_{E1}$  band shifts reversely on compression (Figures 4b and 5d). In the entire pressure range, the pressure coefficients of the  $\nu_{E2}$  mode is  $\sim 2.5 \text{ cm}^{-1}\cdot\text{GPa}^{-1}$  and of  $\nu_{E3}$  reduces from 5.9(1) at atmospheric pressure slightly to 5.7(2)  $\text{cm}^{-1}\cdot\text{GPa}^{-1}$  at 23.5 GPa. The mode shifts obtained here are in general agreement with those measured in previous studies [20,21], except that the  $\nu_{E3}$  band displays a steeper slope here. Differences in aragonite specimen, pressure medium and pressure range, etc., could account for this discrepancy. In spite of the discrepancy, our study and the previous studies find that the internal modes undergo smaller pressure shifts than the external modes. This indicates that, in comparison with the  $[\text{CO}_3]^{2-}$  units, the  $[\text{CaO}_9]$  polyhedral are more compressible and they bear the compaction of the volume dominantly.

At the molecular level, the site and stability of  $\text{H}^+$  in minerals is dependent upon the bond strength and the local geometry; both are constrained by the co-ordinated polyhedral. Here, we report, for the first time, the existence and evolution of  $\text{H}^+$  within aragonite lattice upon pressure. Firstly, the difference in the shape of the three OH bands (Figure 4a) is attributed to the difference in their chemical and structural environments. This is due to the fact that the  $\text{O}^{2-}$  co-ordinated with  $\text{Ca}^{2+}$  or  $\text{C}^{4+}$  are nonequivalent [33]. Secondly, all the OH modes exhibit a decrease in band wavenumbers with increasing pressure (Figure 4a,e). There are two factors controlling the direction of the shift of the OH mode wavenumbers. For OH modes at higher wavenumbers, the H-bonds are weaker and the blue-shift of the peak position is due dominantly to the compression of the local structure. For OH modes with lower wavenumbers, the H-bonds are stronger and the red-shift of the peak position is controlled mainly by the compression of the H-bond. The pressure shifts of the OH modes are all negative in the present experiment, thereby implying that the compression of the local structure is the dominating process. It is noteworthy that the three OH bands have similar pressure slopes, which implies that the  $\text{H}^+$  within the lattice have OH bonds of similar strength. As pressure is increased to above 11.5 GPa, the three OH bands become unregistered against the background and replaced by a broad band. The emergence of the broad band may be arisen from (1) the orientational disorder of  $\text{H}^+$  in the lattice, (2) a statistical distribution of  $\text{H}^+$  across multiple environments due to the pressure-induced redistribution of  $\text{H}^+$ , (3) the generation of the pressure gradient and/or (4) H-loss upon compression. The third should be excluded because the initial intensity of the OH bands do not come back as pressure is released. If there is no H-loss, the change of the integral absorbance would be a sign of the pressure-dependent absorption coefficient according to Beer–Lambert law.

#### 3.4. Vibrational Spectra of Aragonite above 15 GPa

During further pressure growth to above 14.5 GPa, some anomalies should be noted. The two in-plane bending bands ( $\nu_4$ ) have a pressure shift reduced to approximately 1/3 of those below 14.5 GPa. Specifically, the pressure coefficient reduces from 1.42(1) to 0.54  $\text{cm}^{-1}\cdot\text{GPa}^{-1}$  for 700.21(2)  $\text{cm}^{-1}$  and from 1.95(4) to 0.72  $\text{cm}^{-1}\cdot\text{GPa}^{-1}$  for 712.88(5)  $\text{cm}^{-1}$  (Figure 5a). We acknowledge that a loss of hydrostatic pressure is partly responsible for these mutations. However, the stiffness of the *b*-axis and the discontinuities of the first-order derivatives of the bandwidth and the mode intensity appear consistently at  $\sim 15$  GPa (please see the below) at different pressure medium conditions. Thus, we propose that there appear somewhat structural modifications. Theoretically, in a simple vibrator model, the mode wavenumber is proportional to the square root of force constant. Thus, the mode hardening of  $\nu_4$  reflects that the increased coupling between the  $[\text{CO}_3]^{2-}$  units more than counterbalances the increase in the normal force constant of the bending vibration above 14.5 GPa. Concurrently, the pressure shifts of the out-of-plane bending bands ( $\nu_2$ ), 842.36(3) and 856.47(3)  $\text{cm}^{-1}$ ,

change from  $-0.18$  to  $0.26$  and  $-0.45$  to  $0.12$ , respectively (Figure 5b). In contrast, the band with the highest wavenumber,  $868.87(2) \text{ cm}^{-1}$ , becomes more sensitive to pressure with a negative dependence of  $-0.15 \text{ cm}^{-1} \cdot \text{GPa}^{-1}$ . This implies that there generates more anisotropic strength in the connected Ca-O bonds. There are only two external modes that could be reliably measured here, but Gillet et al. [21] have plotted pressure dependence of five external modes of aragonite. These modes show increases in mode wavenumbers upon pressure along various (linear or quadratic) slopes, which also indicate that the Ca-O bonds turn to be more anisotropic upon pressure. We notice that, in Gillet et al. [20], the mode wavenumber of the  $209 \text{ cm}^{-1}$  band becomes fluctuated violently in the pressure range of 10–20 GPa. This is not detected here. We have no simple explanation for this phenomenon, but note that the solidification of the pressure medium could matter or it may indicates somewhat changes in the Ca-O bonds.

Perhaps the most notable aspect of the vibrational spectra is the variations of the FWHM and the intensity of the modes against pressure (Figure 6). With pressure increment to 13.4 GPa, the two  $\nu_4$  bands exhibit a substantial growth in the magnitude of the bandwidth (increase by a value of  $\sim 20 \text{ cm}^{-1}$ ) and a substantial decrease in the intergal absorbance (by a factor of  $\sim 5$ ). But as the pressure further increases (from 14.5 to 21.5 GPa), the bandwidth and the intensity become almost unchanged (Figure 6a,c). Meanwhile, the width of the diagnostic band of the  $[\text{CO}_3]^{2-}$  unit,  $\nu_1$ , initially increasing gently as pressure increases, becomes broader and broader in a much more progressive way above 14.2 GPa (Figure 6b). Concomitantly, the pressure–width relation of the  $\nu_{E2}$  and  $\nu_{E3}$  bands displays a turning point from a gentle variation to a dramatic increase. These anomalies imply that, above 14.2 GPa, a growing anisotropic behavior occurs in the C-O bonds. Another anomaly lies in the pressure–dependence of the  $\nu_{E2}$  and  $\nu_{E3}$  band intensities, which change from a decreasing trend to an increasing trend at 14.2 GPa (Figure 6d). The continuous increase in intensity may be originated, at least partly, from the strengthened interaction of the corresponding Ca-O bonds upon pressure.

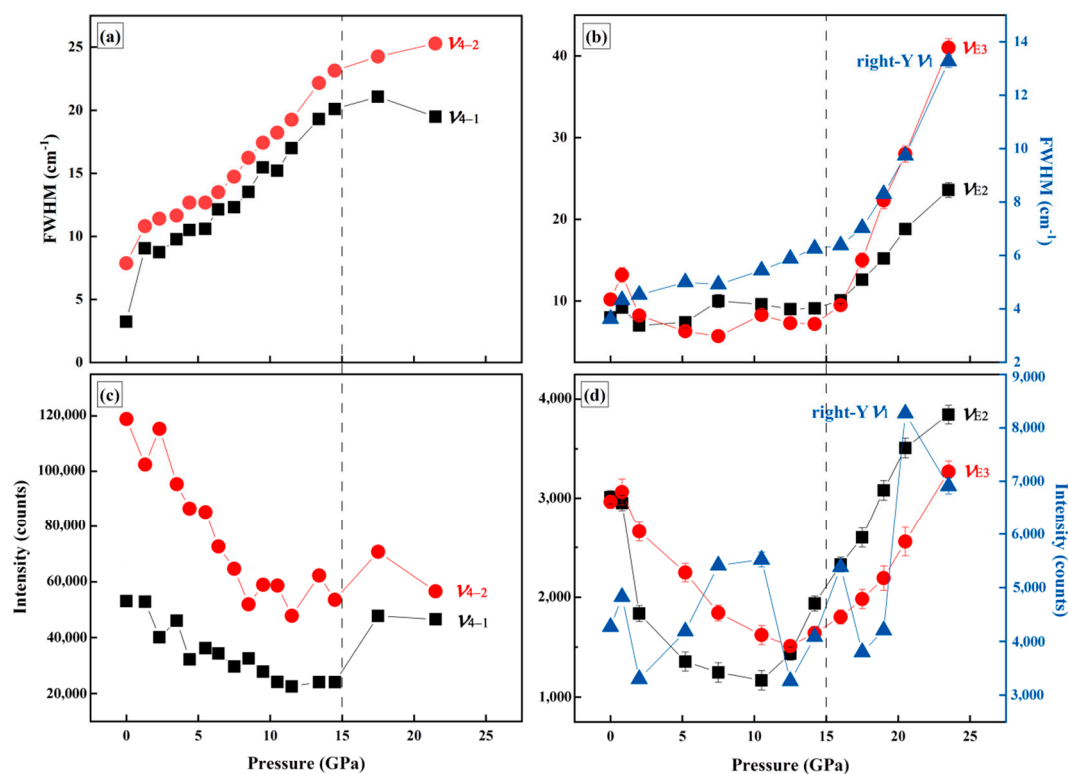


**Figure 6.** (a,b) FWHM and (c,d) intensity of selected IR or Raman modes of aragonite versus pressure with appropriate error bars shown.

### 3.5. Vibrational Spectra of Aragonite upon Decompression

In the course of decompression, the mode wavenumbers return to their initial values at corresponding rates after delay of the order of 30 min. Compared with the initial spectra, there are an intensity loss and a moderate increase in the bandwidth (Figure 4). This reflects that the inter-bonding within the  $[\text{CO}_3]^{2-}$  units has changed upon pressure. Besides, the weakening of the intensity of the OH bands is irreversible, implying that the  $\text{H}^+$  redistribution or disorder retains upon decompression.

### 3.6. Mode Grüneisen Parameters

In the light of the mode pressure coefficients ( $\delta_v/\delta_p$ ) and the bulk modulus ( $B_0 = 71(5)$  GPa), the mode Grüneisen parameters ( $\gamma$ ) of aragonite are readily obtained through  $\gamma_i = (B_0/\nu_{i0})(\delta_v/\delta_p)$ , where  $\nu_{i0}$  is the wavenumber of the  $i$  mode at ambient conditions (Table 4). The internal modes exhibit significantly lower  $\gamma$  values (0.0008–0.24) relative to those of the external modes (1.16 and 2.03), and this is consistent with the results of Kraft et al. [20]. This reflects that the compression of the aragonite volume is mainly attributed to the reduction of the  $[\text{CaO}_9]$  polyhedra. Similar results have been observed in carbonate minerals previously [21,44]. Furthermore, the pressure slopes of the modes below  $\sim 15$  GPa and above  $\sim 15$  GPa are used, respectively, for the calculation. The  $\gamma$  values of the in-plane bending modes dramatically decrease, from 0.14 to 0.05 for the  $700.21(2)$   $\text{cm}^{-1}$  band and from 0.19 to 0.07 for  $712.88(5)$   $\text{cm}^{-1}$ . The  $\gamma$  values of the out-of-plane bending modes also changed. In contrast, the two external modes remain similar  $\gamma$  values in the entire pressure cycle. This reflects that the  $[\text{CO}_3]^{2-}$  units have become very rigid upon pressure, whereas the  $[\text{CaO}_9]$  polyhedra experience considerable compression.

**Table 4.** Vibrational modes for aragonite, their pressure dependences  $\beta$  and the calculated mode Grüneisen parameters.

Modes	$\nu_0$ ( $\text{cm}^{-1}$ )	$\beta$ ( $\text{cm}^{-1}\cdot\text{GPa}^{-1}$ )		$\gamma_i$ ( $B_0 = 71$ GPa)		Assignments
		<15 GPa	>15 GPa	<15 GPa	>15 GPa	
$\nu_{4-1}$	700.2(1)	1.42(1)	0.54	0.14	0.05	C-O in-plane bending
$\nu_{4-2}$	712.8(1)	1.95(4)	0.72	0.19	0.07	
$\nu_{2-1}$	842.3(1)	−0.18(4)	0.26	0.01	0.02	C-O out-of-plane bending
$\nu_{2-2}$	856.4(1)	−0.45(6)	0.12	0.03	0.009	
$\nu_{2-3}$	868.8(1)	−0.01(3)	0.15	0.0008	0.01	
$\nu_1$	1082.19(1)	3.72(9)	3.6(1)	0.24	0.23	C-O symmetrical stretching
$\nu_{E2}$	152.8(1)	2.5(1)	2.5(2)	1.16	1.16	External vibration
$\nu_{E3}$	205.5(1)	5.9(1)	5.7(2)	2.03	1.96	

$\nu_{i0}$ : Initial wavenumber ( $\text{cm}^{-1}$ ) of a vibrational mode at atmospheric pressure.  $\beta = \delta_v/\delta_p$ : Pressure dependence of a mode at room temperature in  $\text{cm}^{-1}\cdot\text{GPa}^{-1}$ . Linear shifts of  $\nu_2$  and  $\nu_4$  are derived from the infrared spectra and of  $\nu_1$  and  $\nu_E$  from a quadratic fit to the Raman data. The error is given in the bracket.  $\gamma_i$ : Mode Grüneisen parameters are calculated by  $\gamma_i = (B_0/\nu_i)(\delta_v/\delta_p)$  considering  $B_0 = 71(5)$  GPa.

## 4. Concluding Remarkings

The structural stability and phase transition of aragonite upon pressure is an unending hot topic of research. The present study has generated a novel vibrational spectroscopic picture of aragonite with discontinuities of the first-order derivatives of the vibrational modes occurring at  $\sim 15$  GPa. We note that these anomalies beginning at  $\sim 15$  GPa involve only O-C-O bending modes, which possibly indicates a second-order phase transition. The appearance of such discontinuities is likely to be related to the reduction of the  $b$ -axis compressibility of aragonite at  $\sim 15$  GPa. As is known, the aragonite structure bears a great degree of compression upon pressure, which is dominantly due to the reduction of the  $[\text{CaO}_9]$  polyhedra. The  $[\text{CO}_3]^{2-}$  units are compressed slightly and grow more distorted because the O-C-O undergo unidentical angular variations [20,33,38]. The present results indicate an abrupt change occurs in the force constant within the  $[\text{CO}_3]^{2-}$  units above  $\sim 15$  GPa. Besides,

the  $[\text{CaO}_9]$  polyhedra begin to deform, with some of the Ca-O bonds becoming elongated and the others shortening. Accordingly, we expect an increased co-ordination number for the  $\text{Ca}^{2+}$  sites at higher pressures. This would be bond to trigger a phase transition under higher pressures. However, the phase transition of aragonite is always accompanied with the displacement of the  $[\text{CO}_3]^{2-}$  units along a direction parallel to the plane of the  $[\text{CO}_3]^{2-}$  units or the rotation of the  $[\text{CO}_3]^{2-}$  units around an axis that is perpendicular to the  $[\text{CO}_3]^{2-}$  units. Displacement or rotation of  $[\text{CO}_3]^{2-}$  confronts a spatial hindrance and repulsion between coplanar the  $[\text{CO}_3]^{2-}$  units. Therefore, it would overcome a certain of kinetic barriers if aragonite transforms to another stable polymorph. Considerable compaction of the  $[\text{CaO}_9]$  polyhedra along the *c*-axis will push  $\text{O}^{2-}$  toward the O-C-O angle, leading to weakened bond strength within the  $[\text{CO}_3]^{2-}$  units [33]. This is favorable for the  $[\text{CO}_3]^{2-}$ -triangles transformation to  $[\text{CO}_4]^{4-}$ -tetrahedra [33,46].

So far, there have been limited studies on the presence of  $\text{H}^+$  within the lattice of carbonate minerals. However, recent findings on inclusions in sublithospheric diamonds have strongly evidenced the associations between carbon and water recycle in the deep earth [13–16]. In the present study, we firstly confirm the difference in the chemical and structural environments of the  $\text{H}^+$  sites in aragonite lattice. Besides, the negative correlation between the wavenumbers of the OH modes and pressure indicates that the compression of the surrounding crystal structure rather than the H-bond is a main process upon compression. We consider that the different compressibilities of the C-O and Ca-O bonds could induce  $\text{H}^+$  redistribution or disorder in the lattice. This is an irreversible process. Alternatively, the weakening of the OH modes above 11.5 GPa may imply  $\text{H}^+$ -loss. The limited data of the infrared spectra above 11.5 GPa have left this inference unconstrained and more studies are needed to verify this hypothesis.

Even though aragonite has long been considered a stable phase in the bulk of the upper-mid mantle [18], the density of aragonite is suggested to be lower than that of principle constituents of the mantle [48]. This casts doubts on the possibility of aragonite in deep zones. Besides, only a trace of calcium carbonate minerals has been recovered from sublithospheric diamonds in comparison with the estimated carbon flux subducted into the Earth [13–16]. Here, we provide a host of arguments for the following fact: the stiffness of the *b*-axis occurring at ~15 GPa (corresponding to the pressure at the bottom of the upper mantle) results in an incompressible structure of aragonite, which may keep it, to a certain degree, from further sinking. Other processes, such as decarbonation, dissolution and metamorphic reactions, etc., are also responsible for the diminished content of aragonite in the lower mantle.

**Author Contributions:** Conceptualization, methodology, formal analysis, data curation, project administration, funding acquisition, writing-original draft: J.G.; formal analysis, data curation, project administration, investigation, validation, visualization, writing-review and editing: Y.L. (Yungui Liu), X.W., Y.L. (Yingxin Liu) and W.S. Investigation, writing-review and editing: X.Y. All authors have read and agreed to the published version of the manuscript.

**Funding:** This study is supported by National Key Research and Development Program of China (Grant no 2018YFA 0702601), Natural Science Foundation of China (Grant no 41902035, 41490614 and 41822202) and China Postdoctoral Science Foundation (Grant no 2018M640179 and 2019T120132). Synchrotron XRD experiments undertaken at the beamline 13-BM-C of APS, is funded by National Science Foundation of China (Grant no 41827802).

**Acknowledgments:** We are grateful to Minghui Li, a professor at ITPCAS, for her help in the identification of the sample structure using the XRD technique. The scientist at beamline 13-BM-C of APS, Dongzhou Zhang, is acknowledged for his technical help in XRD measurements. We deeply appreciate the assistance of Sergey Tkachev for Ne gas loading into the cell. Besides, we offer our heartfelt thanks to Wanghua Wu, a scientist at WITec (Beijing, China) Scientific Technology Co., Ltd., for his advice and help in Raman spectroscopy experiments. The assistance from Xiaoguang Li and Fei Chen for FTIR measurements is acknowledged.

**Conflicts of Interest:** The authors declare no conflict of interest.

## References

1. Oreskes, N. *Plate Tectonics: An Insider's History of the Modern Theory of the Earth*; Westview Press: Boulder, CO, USA, 2001; p. 424.
2. Nippres, S.E.J.; Kuszniir, N.J.; Kendall, J.M. Modeling of lower mantle seismic anisotropy beneath subduction zones. *Geophys. Res. Lett.* **2004**, *31*, L19612. [[CrossRef](#)]
3. Walter, M.J.; Kohn, S.C.; Araujo, D.; Bulanova, G.P.; Smith, C.B.; Gaillou, E.; Wang, J.; Steele, A.; Shirey, S.B. Deep mantle cycling of oceanic crust: Evidence from diamonds and their mineral inclusions. *Science* **2011**, *334*, 54–57. [[CrossRef](#)] [[PubMed](#)]
4. Marty, B.; Jambon, A.  $C^3He$  in volatile fluxes from the solid Earth: Implications for carbon geodynamics. *Earth Planet. Sci. Lett.* **1987**, *83*, 16–26. [[CrossRef](#)]
5. Luth, R.W. Carbon and carbonates in the mantle. *Geochem. Soc. Spec. Pub.* **1999**, *6*, 297–316.
6. Bataleva, Y.V.; Kruk, A.N.; Novoselov, I.D.; Furman, O.V.; Palyanov, Y.N. Decarbonation reactions involving ankerite and dolomite under upper mantle P,T-parameters: Experimental modeling. *Mineral* **2020**, *10*, 715. [[CrossRef](#)]
7. Hammouda, T.; Keshav, S. Melting in the mantle in the presence of carbon: Review of experiments and discussion on the origin of carbonatites. *Chem. Geol.* **2015**, *418*, 171–188. [[CrossRef](#)]
8. Zheng, Y.F.; Chen, R.X.; Xu, Z.; Zhang, S.B. The transport of water in subduction zones. *Sci. China Earth Sci.* **2016**, *59*, 651–682. [[CrossRef](#)]
9. Dasgupta, R.; Hirschmann, M.M.; Withers, A.C. Deep global cycling of carbon constrained by the solidus of anhydrous, carbonated eclogite under upper mantle conditions. *Earth Planet. Sci. Lett.* **2004**, *227*, 73–85. [[CrossRef](#)]
10. Yang, Z.; He, X. Oceanic crust in the mid-mantle beneath west-central Pacific subduction zones: Evidence from S to P converted waveforms. *Geophys. J. Int.* **2015**, *203*, 541–547. [[CrossRef](#)]
11. Bayarjargal, L.; Fruhner, C.-J.; Schrodt, N.; Winkler, B.  $CaCO_3$  phase diagram studied with Raman spectroscopy at pressures up to 50 GPa and high temperatures and DFT modeling. *Phys. Earth Planet. Inter.* **2018**, *281*, 31–45. [[CrossRef](#)]
12. Kaneshima, S. Seismic scatterers in the mid-lower mantle. *Phys. Earth Planet. Inter.* **2016**, *257*, 105–114. [[CrossRef](#)]
13. Brenker, F.E.; Vollmer, C.; Vincze, L.; Vekemans, B.; Szymanski, A.; Janssens, K.; Szaloki, I.; Nasdala, L.; Joswig, W.; Kaminsky, F. Carbonates from the lower part of transition zone or even the lower mantle. *Earth Planet. Sci. Lett.* **2007**, *260*, 1–9. [[CrossRef](#)]
14. Bulanova, G.P.; Walter, M.J.; Smith, C.B.; Kohn, S.C.; Armstrong, L.S.; Blundy, J.; Gobbo, L. Mineral inclusions in sublithospheric diamonds from Collier 4 kimberlite pipe, Juina, Brazil: Subducted protoliths, carbonated melts and primary kimberlite magmatism. *Contrib. Mineral. Petr.* **2010**, *159*, 489–510. [[CrossRef](#)]
15. Dade, P.M.; Harris, J.W. Syngenetic inclusion bearing diamonds from the Letseng-la-Terai, Lesotho. *Agora Political Sci. Undergrad. J.* **1998**, *7*, 561–563.
16. Sobolev, N.V.; Kaminsky, F.V.; Griffin, W.L.; Yefimova, E.S.; Win, T.T.; Ryan, C.G.; Botkunov, A.I. Mineral inclusions in diamonds from the Sputnik kimberlite pipe, Yakutia Source. *Lithos* **1997**, *39*, 135–157. [[CrossRef](#)]
17. Oganov, A.R.; Glass, C.W.; Ono, S. High-pressure phases of  $CaCO_3$ : Crystal structure prediction and experiment. *Earth Planet. Sci. Lett.* **2006**, *241*, 95–103. [[CrossRef](#)]
18. Oganov, A.R.; Ono, S.; Ma, Y.M.; Glass, C.W.; Garcia, A. Novel high-pressure structures of  $MgCO_3$ ,  $CaCO_3$  and  $CO_2$  and their role in Earth's lower mantle. *Earth Planet. Sci. Lett.* **2008**, *273*, 38–47. [[CrossRef](#)]
19. Vizgirda, J.; Ahrens, T.J. Shock compression of aragonite and implications for the equation of state of carbonates. *J. Geophys. Res. Solid Earth* **1982**, *87*, 4747–4758. [[CrossRef](#)]
20. Kraft, S.; Knittle, E.; Williams, Q. Carbonate stability in the Earth's mantle: A vibrational spectroscopic study of aragonite and dolomite at high pressures and temperatures. *J. Geophys. Res.* **1991**, *96*, 17997–18009. [[CrossRef](#)]
21. Gillet, P.; Biellmann, C.; Reynard, B.; McMillan, P. Raman-spectroscopic studies of carbonates Part I: High-pressure and high-temperature behavior of calcite, magnesite, dolomite and aragonite. *Phys. Chem. Miner.* **1993**, *20*, 1–18. [[CrossRef](#)]
22. Pickard, C.J.; Needs, R.J. Structures and stability of calcium and magnesium carbonates at mantle pressures. *Phys. Rev.* **2015**, *B91*, 104101. [[CrossRef](#)]

23. Santillán, J.; Williams, Q. A high pressure X-ray diffraction study of aragonite and the post-aragonite phase transition in CaCO<sub>3</sub>. *Am. Mineral.* **2004**, *89*, 1348–1352. [[CrossRef](#)]
24. Ono, S.; Kikegawa, T.; Ohishi, Y.; Tsuchiya, J. Post-aragonite phase transformation in CaCO<sub>3</sub> at 40 GPa. *Am. Mineral.* **2005**, *90*, 667–671. [[CrossRef](#)]
25. Sekkal, W.; Taleb, N.; Zaoui, A.; Shahrour, I. A lattice dynamical study of the aragonite and post-aragonite phases of calcium carbonate rock. *Am. Mineral.* **2008**, *93*, 1608–1612. [[CrossRef](#)]
26. Gavryushkin, P.N.; Martirosyan, N.S.; Inerbaev, T.M.; Popov, Z.I.; Rashchenko, S.V.; Likhacheva, A.Y.; Lobanov, S.S.; Goncharov, A.F.; Prakapenka, V.B.; Litasov, K.D. Aragonite-II and CaCO<sub>3</sub>-VII: New high-pressure, high-temperature polymorphs of CaCO<sub>3</sub>. *Cryst. Growth Des.* **2017**, *17*, 6291–6296. [[CrossRef](#)]
27. Li, X.Y.; Zhang, Z.G.; Lin, J.F.; Ni, H.W.; Prakapenka, V.B.; Mao, Z. New high pressure phase of CaCO<sub>3</sub> at the topmost lower mantle: Implication for the deep mantle carbon transportation. *Geophys. Res. Lett.* **2018**, *45*, 1335–1360.
28. Smith, D.; Lawler, K.V.; Martinez-Canales, M.; Daykin, A.W.; Fussell, Z.; Alexander, S.; Childs, C.; Smith, J.S.; Pickard, C.J.; Salamat, A. Postaragonite phases of CaCO<sub>3</sub> at lower mantle pressures. *Phys. Rev. Mater.* **2018**, *2*, 013605. [[CrossRef](#)]
29. Zhang, Z.G.; Mao, Z.; Liu, X.; Zhang, Y.G.; Brodholt, J. Stability and reactions of CaCO<sub>3</sub> polymorphs in the Earth's deep mantle. *J. Geophys. Res. Sol. Earth* **2018**, *123*, 6491–6500. [[CrossRef](#)]
30. Gonzalez-Platas, J.; Muñoz, A.; Rodríguez-Hernandez, P.; Errandonea, D. High-pressure single-crystal X-ray diffraction of lead chromate: Structural determination and reinterpretation of electronic and vibrational properties. *Inorg. Chem.* **2019**, *58*, 5966–5979. [[CrossRef](#)]
31. Gonzalez-Platas, J.; Lopez-Moreno, S.; Bandiello, E.; Bettinelli, M.; Errandonea, D. Precise characterization of the rich structural landscape induced by pressure in multifunctional FeVO<sub>4</sub>. *Inorg. Chem.* **2020**, *59*, 6623–6630. [[CrossRef](#)]
32. Merlini, M.; Hanfland, M.; Crichton, W.A. CaCO<sub>3</sub>-III and CaCO<sub>3</sub>-VI, high-pressure polymorphs of calcite: Possible host structures for carbon in the Earth's mantle. *Earth Planet. Sci. Lett.* **2012**, *333–334*, 265–271. [[CrossRef](#)]
33. Palaich, S.E.M.; Heffern, R.A.; Hanfland, M.; Lausi, A.; Kavner, A.; Manning, C.E.; Merlini, M. High-pressure compressibility and thermal expansion of aragonite. *Am. Mineral.* **2016**, *101*, 1651–1658. [[CrossRef](#)]
34. Katsura, T.; Yoneda, A.; Yamazaki, D.; Yoshino, T.; Ito, E. Adiabatic temperature profile in the mantle. *Phys. Earth Planet. Inter.* **2010**, *183*, 212–218. [[CrossRef](#)]
35. Carteret, C.; De La Pierre, M.; Dossot, M.; Pascale, F.; Erba, A.; Dovesi, R. The vibrational spectrum of CaCO<sub>3</sub> aragonite: A combined experimental and quantum-mechanical investigation. *J. Chem. Phys.* **2013**, *138*, 014201. [[CrossRef](#)] [[PubMed](#)]
36. Martinez, I.; Zhang, J.Z.; Reeder, R.J. In situ X-ray diffraction of aragonite and dolomite at high pressure and high temperature: Evidence for dolomite breakdown to aragonite and magnesite. *Am. Mineral.* **1996**, *81*, 611–624. [[CrossRef](#)]
37. Ye, Y.; Smyth, J.R.; Boni, P. Crystal structure and thermal expansion of aragonite-group carbonates by single-crystal X-ray diffraction. *Am. Mineral.* **2012**, *97*, 707–712. [[CrossRef](#)]
38. Li, Y.; Zou, Y.T.; Chen, T.; Wang, X.B.; Qi, X.T.; Chen, H.Y.; Du, J.G.; Li, B.S. P-V-T equation of state and high-pressure behavior of CaCO<sub>3</sub> aragonite. *Am. Mineral.* **2015**, *100*, 2323–2329. [[CrossRef](#)]
39. Liu, L.G.; Chen, C.; Lin, C.C.; Yang, Y.J. Elasticity of single-crystal aragonite by Brillouin spectroscopy. *Phys. Chem. Miner.* **2005**, *32*, 97–102. [[CrossRef](#)]
40. Holmes, N.C.; Moriarty, J.A.; Gathers, G.R.; Nellis, W.J. The equation of state of platinum to 660 GPa (6.6 Mbar). *J. Appl. Phys.* **1989**, *66*, 2962–2967. [[CrossRef](#)]
41. Mao, H.K.; Xu, J.A.; Bell, P.M. Calibration of the ruby pressure gauge to 800 kbar. *J. Geophys. Res.* **1986**, *91*, 4673–4676. [[CrossRef](#)]
42. Rivers, M.; Prakapenka, V.B.; Kubo, A.; Pullins, C.; Holl, C.M.; Jacobsen, S.D. The COMPRES/GSECARS gas-loading system for diamond anvil cells at the Advanced Photon Source. *High Press. Res.* **2008**, *28*, 273–292. [[CrossRef](#)]
43. Errandonea, D.; Muñoz, A.; Gonzalez-Platas, J. Comment on “High-pressure x-ray diffraction study of YBO<sub>3</sub>/Eu<sup>3+</sup>, GdBO<sub>3</sub>, and EuBO<sub>3</sub>: Pressure-induced amorphization in GdBO<sub>3</sub>”. *J. Appl. Phys.* **2014**, *115*, 216101. [[CrossRef](#)]

44. Serghiou, G. High-pressure phase transitions in tetrahedrally coordinated chain structures. *J. Raman Spectrosc.* **2016**, *47*, 1247–1258. [[CrossRef](#)]
45. White, W.B. The Carbonate Minerals. In *The Infrared Spectra of Minerals*; Farmer, V.C., Ed.; Mineralogical Society Monograph: London, UK, 1974; pp. 227–279.
46. Boulard, E.; Pan, D.; Galli, G.; Liu, Z.X.; Mao, W.L. Tetrahedrally coordinated carbonates in Earth's lower mantle. *Nat. Commun.* **2015**, *6*, 6311. [[CrossRef](#)]
47. Ding, S.L. Study on Fourier Transform Infrared Spectroscopy of Natural Ceramic Biogenic Aragonite. Master's Thesis, Guangxi University, Nanning, China, 2006.
48. Litasov, K.D.; Ohtani, E.; Ghosh, S.; Suzuki, A.; Funakoshi, K. Thermal equation of state of superhydrous phase B to 27 GPa and 1373 K. *Phys. Earth Planet. Inter.* **2007**, *164*, 142–160. [[CrossRef](#)]

**Publisher's Note:** MDPI stays neutral with regard to jurisdictional claims in published maps and institutional affiliations.



© 2020 by the authors. Licensee MDPI, Basel, Switzerland. This article is an open access article distributed under the terms and conditions of the Creative Commons Attribution (CC BY) license (<http://creativecommons.org/licenses/by/4.0/>).